**RESEARCH ARTICLE**

# Event-based precipitation characteristics related to cloud-top temperature during pre-summer rainy season over south China

Aoqi Zhang[1,2] | Yilun Chen[1,2] | Weibiao Li[1,2] | Shumin Chen[2]

[1]School of Atmospheric Sciences and Key Laboratory of Tropical Atmosphere-Ocean System, Ministry of Education, Sun Yat-Sen University, Zhuhai, China

[2]Southern Marine Science and Engineering Guangdong Laboratory (Zhuhai), Zhuhai, China

**Correspondence**
Yilun Chen, School of Atmospheric Sciences and Key Laboratory of Tropical Atmosphere-Ocean System, Ministry of Education, Sun Yat-Sen University, Zhuhai, China.
Email: chenylun3@mail.sysu.edu.cn

**Abstract**

Precipitation exists in the form of event, which means all pixels within the same event have similar atmospheric condition and development experiences. Therefore, using GPM DPR and Himawari-8 AHI data from 2016 to 2020, we carried out event-based investigations on precipitations during the pre-summer rainy season over south China. The identified rain clusters (RCs) were classified into three classes based on the mode of cloud-top temperature, including those <230, 230–265, and >265 K. The results show that RCs with mode of cloud-top temperature <230 K were related to low-level velocity and jet. The atmospheric layer was very unstable with sufficient moisture supply, so the ratio of convective precipitation reached as high as 20% with largest droplet size. RCs at 230–265 K were mainly frontal stratiform precipitations caused by quasi-stationary front. The atmospheric layer was stable but the horizontal moisture flux was strong; precipitations often appeared as continuous light rain with high droplet density and small droplet size. RCs with mode of cloud-top temperature >265 K contributed less than 10% of the accumulated rainfall amount. They were mainly warm-cloud shallow precipitations triggered by local convection with low droplet density. Our results suggest that the event-scale characteristics of precipitation are indicative of the triggers and microphysics of precipitation.

**KEYWORDS**

atmospheric condition, cloud-top temperature, precipitation microphysics, rain clusters, south China

## 1 | INTRODUCTION

The pre-summer rainy season, also called the pre-flood season, usually lasts from April to June and is one of the two prominent rainfall seasons over south China (Tao and Chen, 1987). During the pre-summer rainy season, the accumulated rainfall amount accounts for 40–60% of the annual rainfall amount over south China (Luo et al., 2017). Different from the typhoon precipitations in July–October, the rainfall during the pre-summer rainy season over south China is usually related to the East Asia summer monsoon and the westerlies with relatively stable large-scale background (Ding and Chan, 2005). Therefore, meso- and small-scale disturbances such as topography, low-level jet (LLJ), and land–sea thermodynamics play key roles in the triggering of precipitation during the pre-summer rainy season (Jiang et al., 2017; Bai et al., 2020).

With the vigorous development of observation instruments and research methods in the past 20 years, there have been numerous progresses on the characteristics of precipitation during the pre-summer rainy season over south China (Sun et al., 2019; Luo et al., 2020). In terms of temporal variation, Curtis (2019) used Global Precipitation Climatology Centre (GPCP) gridded product and pointed out that the precipitation in the coastal areas of continent showed an insignificant upward trend under the background of global climate change. There was also similar long-term trend for extreme precipitation over south China (Gu et al., 2017; Zhang et al., 2017). Using rain gauge observations, Yu et al. (2007) conducted a series of studies on the diurnal variation characteristics of regional precipitation in China and pointed out that summer precipitation in south China presents an obvious afternoon peak, which should be related to the diurnal variation of monsoon activity (Chen et al., 2009; Du and Rotunno, 2018).

In terms of precipitation triggers, the heavy rainfall over south China during the pre-summer rainy season mainly contains the frontal heavy rainfall and the warm-sector heavy rainfall (Wu et al., 2020; Li and Du, 2021). The frontal precipitations are related to the dynamic forcing of quasi-stationary front (similar to meiyu front) and cold front over south China (Tao and Chen, 1987; Han et al., 2021). The triggering mechanisms of warm-sector heavy rainfall are very complex, which include the coastal convergence related to LLJ (Du and Chen, 2019), the inhomogeneous underlying surface layer such as topography and land–sea contrast (Xu et al., 2012; Chen et al., 2014), gravity wave (Liu et al., 2012), and atmospheric perturbation instability (Weckwerth and Wakimoto, 1992). Apart from the heavy rainfalls, there are also light rainfalls linked with activities of warm clouds during the pre-summer rainy season over south China (Zheng et al., 2019).

In terms of precipitation microphysics, the relevant studies are still limited. Using combinations from ground-based disdrometer and vertical radar, Huo et al. (2019) statistically analysed the droplet size distribution (DSD) of precipitation in south China from June to July 2016–2017 and established the $D_m$–$N_w$ and $Z$–$R$ relationships for variant types of precipitation. Based on ground-based dual-polarization radar observations during the Southern China Monsoon Rainfall Experiment (SCMREX), Luo et al. (2020) revealed that the extreme rainfall over south China during the pre-summer rainy season is attributed to the active warm rain processes. Han et al. (2021) studied the microphysical characteristics of two coexisting frontal and warm-sector heavy rainfall events over south China, and pointed out the warm-sector event has stronger convection intensity and larger droplet size than frontal event.

The previous statistics on the precipitation characteristics during the pre-summer rainy season over south China were mainly based on the scale of detection pixel or data grid, such as the Tropical Rainfall Measuring Mission (TRMM) Precipitation Radar (PR) pixel with a horizontal resolution of 5 km × 5 km (Li et al., 2019). However, precipitation does not exist as a single pixel but in the form of system (event)—a single precipitation event may contain thousands of pixels (Liu and Zipser, 2015; Fu et al., 2021). The precipitation pixels within the same precipitation event should be under the same atmospheric condition and experience similar development stage, thus we need to study the characteristics of precipitation from the scale of event (Fiolleau and Roca, 2013; Zhang et al., 2022). Using combinations from Global Precipitation Mission (GPM) Dual-frequency Precipitation Radar (DPR), Zhang and Fu (2018) investigated the three-dimensional structure and microphysics of precipitations over east China. Chen et al. (2021) studied the structural properties of rain cells (RCs) over the Tibet Plateau. Researches on the precipitation characteristics in south China from the perspective of event can closely link the environmental conditions, macroscale characteristics, and precipitation structure of precipitation.

The relationship between cloud-top temperature and near-surface rain rate has always been a hotspot in the field of satellite remote sensing (Hanna et al., 2008; Lau and Wu, 2010). However, we still do not know how the cloud-top temperature is related to precipitation event over south China during the pre-summer rainy season from the perspective of precipitation events. In this study, we will investigate this issue by using GPM DPR orbital precipitation dataset, Himawari-8 brightness temperature product, and ERA5 reanalysis data. This study consists of four sections. Section 2 illustrates the data usage, identification of RC (precipitation event), and definition of the mode of cloud-top temperature. Section 3 introduces the environmental conditions, horizontal distributions, and microphysics of RCs with different modes of cloud-top temperature. Section 4 is the discussion and conclusions.

## 2 | DATA AND METHODS

### 2.1 | Data

GPM DPR, containing a Ku-band (13.6 GHz) and a Ka-band (35.5 GHz) precipitation radar, covers the world from 65°N to 65°S about 16 times a day. GPM DPR has three scan modes, namely Ku-band normal scan, Ka-band matched scan, and Ka-band high-sensitivity scan, with minimum detectable reflectivity of 15.46, 19.18, and 13.71 dBZ, respectively (Seto et al., 2021). Based on the co-observations

of Ku-band and Ka-band radar, the dual-frequency algorithms were developed to provide users level-2 dual-frequency precipitation product GPM 2ADPR. In this study, we used the GPM 2ADPR product, which contains radar corrected reflectivity, rain type, precipitation phase, rain rate profile, DSD profile, and other precipitation information with a horizontal resolution of 5 km × 5 km and a vertical interval of 125 m. The rain type of precipitation contains stratiform, convective, shallow, and other. As other precipitation account for less than 1% of the total precipitation, it is not specifically presented in the draft.

The cloud-top brightness temperature information used in this study was from the longwave infrared band (10.4 μm) detections of Advanced Himawari Image (AHI) onboard geostationary satellite Himawari-8. The sum of observational and model error variance is about 1 K for this band (Da, 2015). To be consistent with GPM 2ADPR product, we used the Himmawari-8 full-disk cloud-top temperature ($TB_{10.4}$) on 0.05° × 0.05° grids with a temporal resolution of 10 min (http://ftp.ptree.jaxa.jp, last accessed: April 12, 2022).

In addition, we also used geopotential, winds, water vapour flux, and other environmental information from ERA5 dataset on 0.25° × 0.25° grids with a temporal interval of 1 hr (Hersbach et al., 2020). The atmospheric stability and moisture supply are two key environmental conditions in the occurrence and development of precipitation. Therefore, we calculated the average convective available potential energy (CAPE) and integrated water vapour flux ($Q_u$ and $Q_v$). The formulas are as follows:

$$\text{CAPE} = \int_{z_f}^{z_n} g \left( \frac{T_{v,\text{par}} - T_{v,\text{env}}}{T_{v,\text{env}}} \right) dz, \qquad (1)$$

$$Q_u = \int_{p_s}^{p_t} \frac{qu}{g} dp, \qquad (2)$$

$$Q_v = \int_{p_s}^{p_t} \frac{qv}{g} dp, \qquad (3)$$

$$\text{div}\, Q = \nabla \cdot Q = \int_{p_s}^{p_t} \left( \frac{\partial \frac{qu}{g}}{\partial x} + \frac{\partial \frac{qv}{g}}{\partial y} \right) dp, \qquad (4)$$

where $z$ and $p$ indicate atmospheric height and pressure; $z_f$ represents the level of free condensation and $z_n$ indicates the height of equilibrium level; $T_{v,\text{env}}$ and $T_{v,\text{par}}$ are virtual temperature of environment and particle; $p_t$ and $p_s$ are the atmospheric pressure at atmospheric top and surface, respectively; $u$ and $v$ are the components of winds, while $Q_u$ and $Q_v$ are the components of integrated water
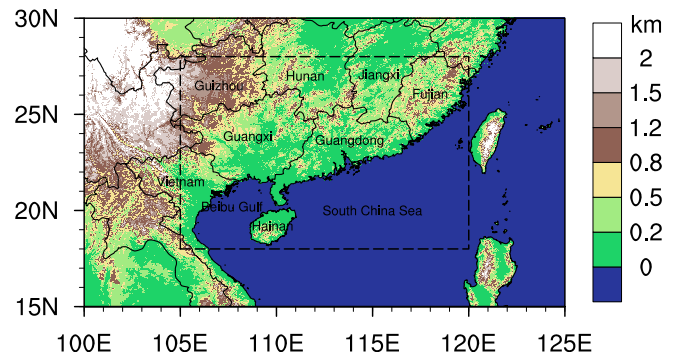


**FIGURE 1** Horizontal distribution of elevation over south China and surrounding regions, derived from NGDC DEM data. The dashed rectangle indicates our study region [Colour figure can be viewed at wileyonlinelibrary.com]

vapour flux; $g$ is the gravitational acceleration; and div $Q$ is the vertical integral of divergence of water vapour flux.

The elevation information with a horizontal resolution of ~3 km was from the Digital Elevation Model (DEM) data provided by the National Geophysical Data Center (NGDC). Considering that GPM DPR works since 2014 and Himawari-8 works since 2016, the study period was set as the pre-summer rainy season in south China (April–June) from 2016 to 2020.

## 2.2 | Study region and identification of RC

Figure 1 shows the horizontal distribution of elevation over south China and surrounding regions. The dashed rectangle indicates our study region (105°–120°E, 18°–28°N), which mainly consists of Guangdong, Guangxi, Fujian, Hainan Island, and Beibu Gulf, and partial regions of Guizhou, Hunan, Jiangxi, South China Sea, and Vietnam. On the land surface in the study area, the terrain height is mainly 0–1.2 km. The undulating hilly terrain of south China plays an important role in the generation and development of the precipitation during the pre-summer rainy season (Ding and Chan, 2005).

We identified RCs from GPM 2ADPR product by grouping contiguous precipitation pixels (near-surface rain rate >0 mm·hr$^{-1}$). Similar identification method has been used in numerous event-based precipitation studies (Nesbitt et al., 2006). All RCs were retained, regardless of whether the RC was truncated by the DPR swath (Zhang et al., 2022). We identified totally 9,573 RCs with 441,261 2ADPR precipitation pixels which were located over the study region (central location) during the pre-summer rainy seasons for 2016–2020.

The Himawari-8 AHI data was matched to DPR pixels within RCs following the closest point principle. The
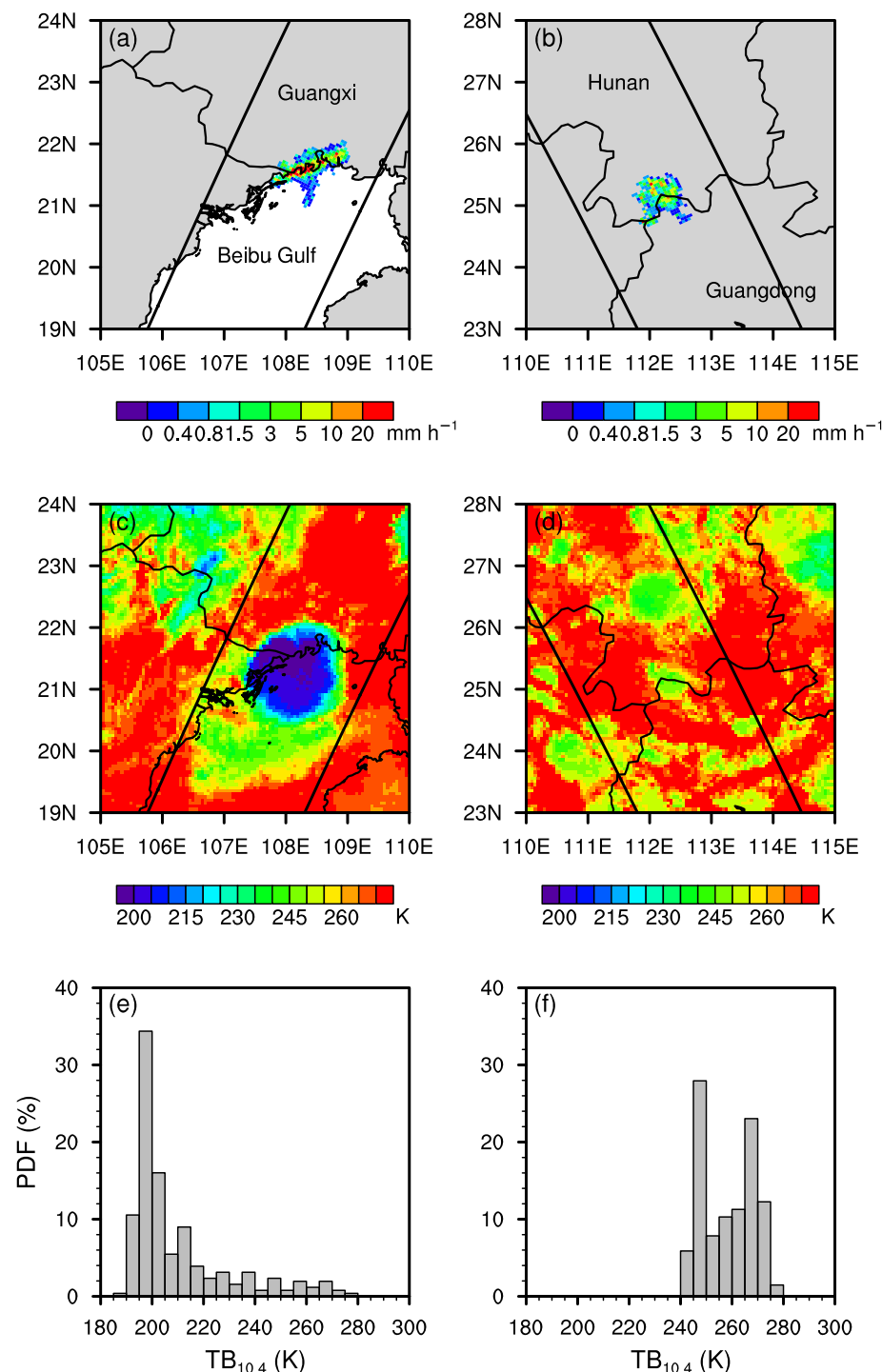
FIGURE 2 The horizontal distributions of (a, b) GPM 2ADPR near-surface rain rate and (c, d) Himawari-8 AHI TB$_{10.4}$, and (e, f) PDFs of TB$_{10.4}$ of precipitation pixels for two different RCs occurring at 2120 UTC June 15, 2019 (left panels) and 1047 UTC April 20, 2018 (right panels), respectively [Colour figure can be viewed at wileyonlinelibrary.com]

time lag of matched Himawari-8 AHI data and RC should be within ±5 min. Specifically, the statistics were derived on 2ADPR pixels of RCs.

## 2.3 | Mode of RC

Figure 2 presented two cases of RCs. The first one occurred over the sea–land junction area of Beibu Gulf

and Guangxi province at 2120 UTC June 15, 2019, which was a typical RC forced by land–sea contrast (Figure 2a). The RC contained 256 DPR precipitation pixels, which were distributed along the coastline like a "strip." The near-surface rain rate increased with decreasing distance from the coastline with a maximum value exceeding 20 mm·hr$^{-1}$ (Figure 2a). Unlike the shape of RC, the corresponding cloud system showed in quasi-circular shape with minimum TB$_{10.4}$ < 200 K (Figure 2c). The area of

**FIGURE 3** Histograms of (a) number, (b) average area, (c) average near-surface rain rate, and (d) rainfall contribution to total precipitation amount for RCs of different mode of $TB_{10.4}$, derived from GPM 2ADPR for the pre-summer rainy season 2016–2020
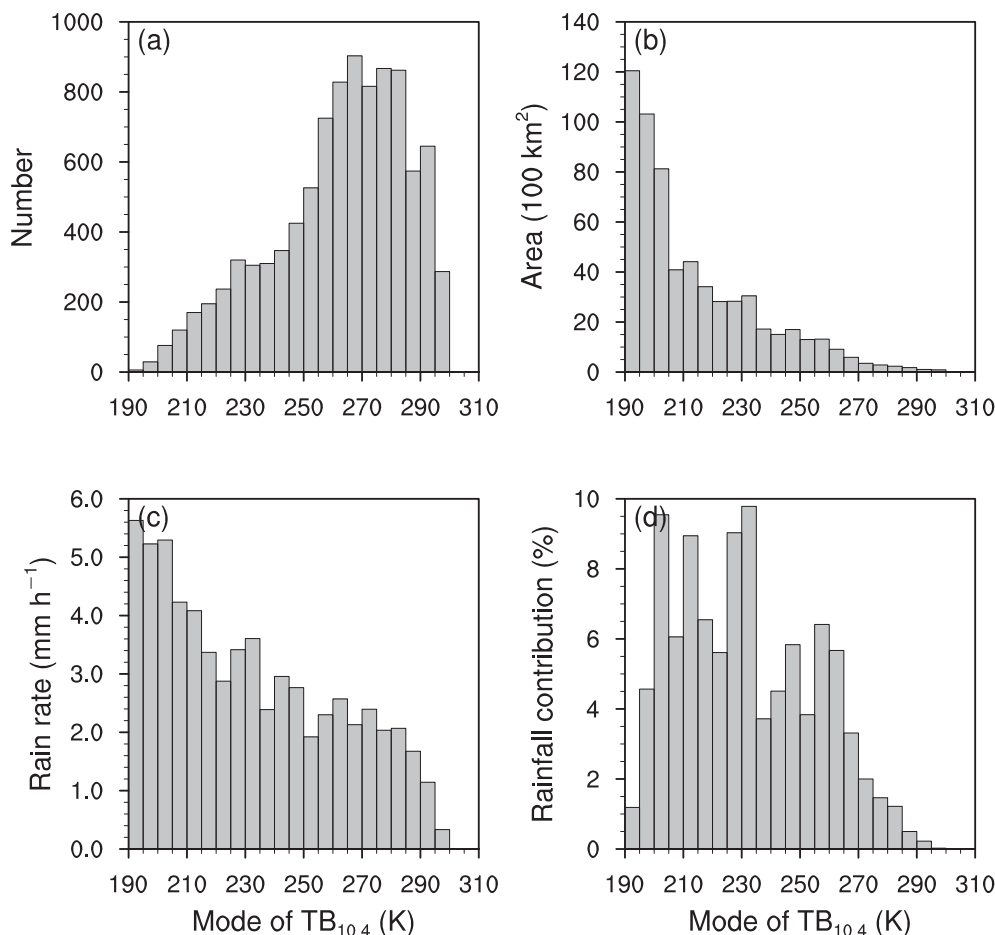


cloud system far exceeded that of RC, indicating most regions within the cloud system were free of precipitation (Figure 2a,c).

The second case occurred over the boundaries of Guangdong province and Hunan province at 1047 UTC April 20, 2018 (Figure 2b), which should be related to the mountain ranges there (Figure 1). This RC contained 204 DPR precipitation pixels and showed in quasi-circular shape (Figure 2b). The near-surface rain rate was mainly distributed in the range of 1.5–5 mm·hr$^{-1}$ with maximum <10 mm·hr$^{-1}$ (Figure 2b). The corresponding cloud system also presented a quasi-circular shape with minimum $TB_{10.4}$ of ~240 K (Figure 2d). The cloud system and RC were similar in both size and shape, indicating that precipitation occurred in most of the cloud system (Figure 2b,d).

The probability distribution functions (PDFs) of $TB_{10.4}$ for precipitation pixels of the two events were shown in Figure 2e,f. We used the mode of $TB_{10.4}$ of RC at 5 K intervals to represent the overall cloud-top temperature. For the first RC, The $TB_{10.4}$ was distributed in the interval of 185–280 K with a peak (hereafter mode) of 195–200 K (Figure 2e). For the second RC, the $TB_{10.4}$ was distributed in the interval of 240–280 K with a mode of 245–250 K (Figure 2f), indicating lower cloud top than the first one.

# 3 | RESULTS

## 3.1 | Classification of RCs

The mode of $TB_{10.4}$ indicates the general cloud-top temperature of RC. To investigate the relationships between cloud-top temperature and precipitation characteristics, we would like to classify the RCs by selecting the thresholds of mode of $TB_{10.4}$. Therefore, we first focused on several basic parameters of RCs related to the mode of $TB_{10.4}$.

The relationships between RC number and mode of $TB_{10.4}$ were showed in Figure 3a. With the increasing of mode of $TB_{10.4}$ till 285 K, RC number showed an almost linear trend with a slope of about 9 K$^{-1}$. RC number peaked at 260–285 K with about 850 RCs in every 5 K interval, indicating that there existed numerous warm-cloud precipitation in the pre-summer rainy season over south China (Zheng *et al.*, 2019). The variation of RC area showed opposite features to RC number—the average RC area decreased exponentially with increasing mode of $TB_{10.4}$ (Figure 3b). In the interval of 190–195 K, the average RC area reached 12,000 km$^2$, which was more than 30 times the average RC area over land
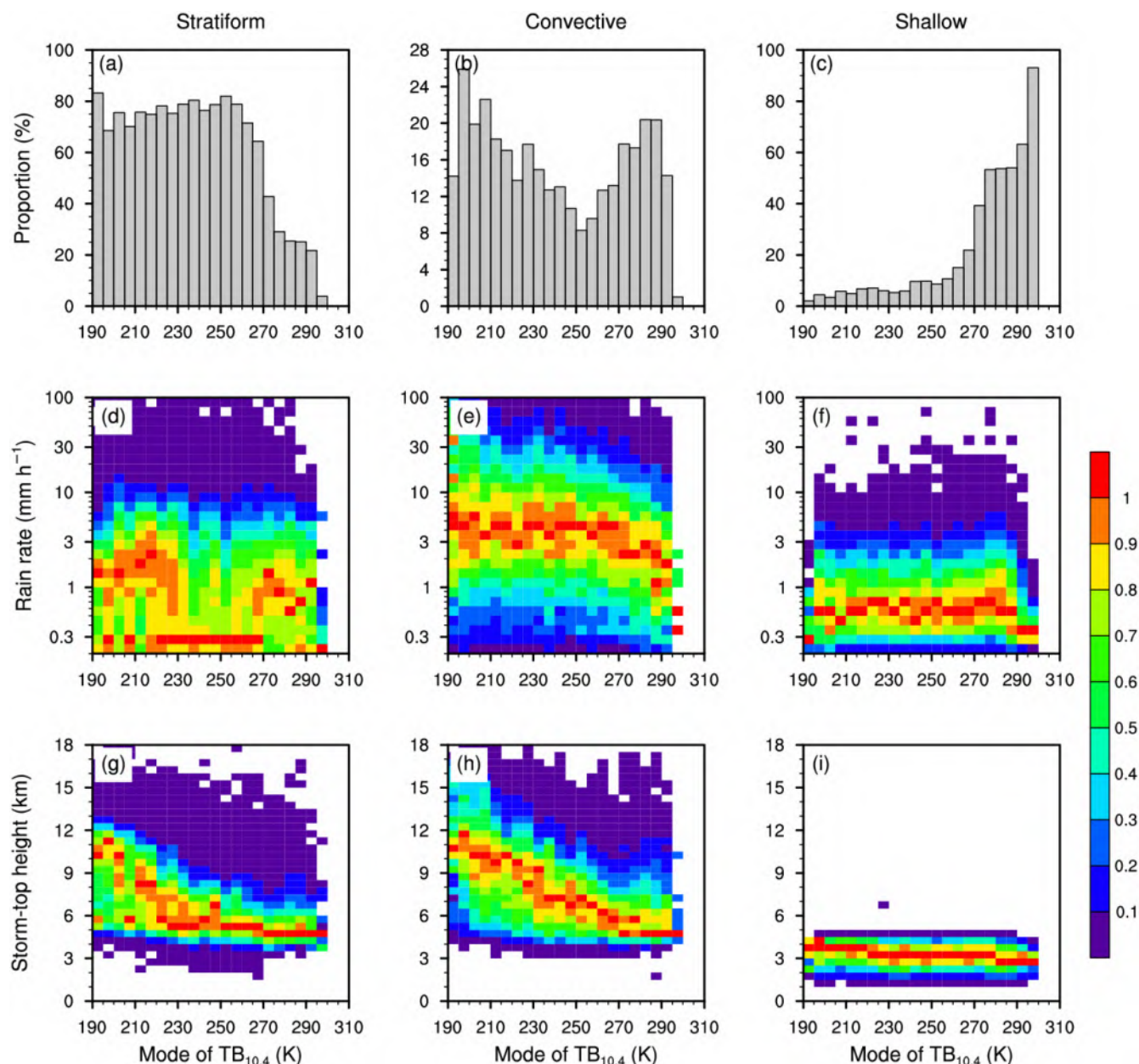
**FIGURE 4** (a–c) Ratio of stratiform, convective, and shallow precipitation for RCs of different mode of $TB_{10.4}$ and two-dimensional PDFs in (d–f) near-surface rain rate and mode of $TB_{10.4}$ and (g–i) storm-top height and mode of $TB_{10.4}$, derived from 2ADPR pixels for different rain types during the pre-summer rainy season 2016–2020. The spacing of near-surface rain rate is ($\Delta lg RR = 0.1$). The spacings of mode of $TB_{10.4}$ and storm-top height are 5 K and 0.5 km, respectively. [Colour figure can be viewed at wileyonlinelibrary.com]

(385 km²; Fu et al., 2021). These RCs often correspond to warm-sector heavy rainfall over coastal regions, which are usually companied with sufficient water vapour flux and intense updraft. Under such excellent environmental condition and the inhomogeneous underlying surface layer especially land–sea contrast (Chen et al., 2014), numerous precipitations intensively occur over the coastal region and form large RC.

The average near-surface rain rate gradually decreased with increasing mode of $TB_{10.4}$ (Figure 3c).

The average rain rate was as high as 5.6 mm·hr⁻¹ in the interval of 190–195 K, whereas <2.5 mm·hr⁻¹ for warm-cloud RCs with mode of $TB_{10.4}$ > 270 K. The rainfall contribution to total precipitation amount was proportional to the product of the above three parameters (Figure 4d). It had two peak intervals at 200–235 and 240–265 K, with average rainfall contribution of about 7.9 and 5.3% per 5 K, respectively.

Figure 4a–c shows the ratio of stratiform, convective, and shallow precipitations for variant mode of $TB_{10.4}$.

These ratios showed as three-segment distributions: (a) For RCs with mode of $TB_{10.4} < 230$ K, the ratio of convective precipitation reached as high as 20%, whereas about 70 and <5% for stratiform and shallow precipitation. (b) For RCs with mode of $TB_{10.4}$ in the range of 230–265 K, the ratio of stratiform precipitation reached 80%, while the ratios of convective and shallow precipitation were both about 10%. (c) For RCs with mode of $TB_{10.4} > 265$ K, the ratio of stratiform precipitation decreased sharply with mode of $TB_{10.4}$, while the ratio of shallow precipitation increased rapidly with mode of $TB_{10.4}$. This is because that the cloud-top height was close to or below the 0°C level for these RCs, which restricts the ice-phased processed within clouds. The ratio of convective precipitation was also as high as 16%, which may be related to the RCs were at development stage at this moment (Zhang and Fu, 2018). The statistics of rain-type properties of warm-cloud RCs showed consistent with that intense warm rain is provided by convective clouds, not by stratiform clouds (Kodama *et al.*, 2009).

Figure 4d–i are the two-dimensional PDFs in near-surface rain rate (or storm-top height) and mode of $TB_{10.4}$. For stratiform precipitations (Figure 4d,g), the two-dimensional PDFs also showed in three-segment distributions. The near-surface rain rate of stratiform precipitation had a mode of 1–2 mm·hr$^{-1}$ for precipitation systems with mode of $TB_{10.4} < 230$ K or >265 K, whereas it was only ~0.3 mm·hr$^{-1}$ for mode of $TB_{10.4}$ at 230–265 K (Figure 4d). The storm-top height of stratiform precipitation rapidly decreased with increasing mode of $TB_{10.4}$ till 230 K, whereas it kept similar for mode of $TB_{10.4} > 230$ K.

For convective precipitations, the near-surface rain rate kept nearly constant with mode of $TB_{10.4} < 265$ K, whereas the near-surface rain rate sharply decreased with increasing mode of $TB_{10.4}$ from 265 K (Figure 4e). This should be due to the moisture supply in precipitation systems were mainly concentrated in low-to-mid atmospheric layers (Rao and Reddy, 2019). The storm-top height decreased with increasing mode of $TB_{10.4}$ from 12 km at 190 K to about 5 km at 265 K, whereas it kept at about 5 km after 265 K (Figure 4h). For shallow precipitations, the near-surface rain rate and storm-top height were less related to mode of $TB_{10.4}$ (Figure 4f,i).

Based on the three-segment distributions of features of RCs related to modes of $TB_{10.4}$, we divided the RCs into three categories with modes of $TB_{10.4}$ at the range of <230, 230–265, and >265 K. The three types of RCs contributed 51.49, 39.77, and 8.74%, respectively, to the total precipitation in south China.

The horizontal distributions of precipitation sample sizes for three classes of RCs were shown in Figure 5. RCs with mode of $TB_{10.4} < 230$ K were mainly concentrated in the offshore areas, so the sample size showed a southwest–northeast distribution (Figure 5a). This class of RCs includes the coastal warm-sector heavy precipitation and inland precipitation formed by strong mesoscale convective systems (MCSs).

The precipitation samples for RCs with mode of $TB_{10.4}$ at the range of 230–265 K were concentrated in the inland area of 23°–27°N, showing an east–west rainband, which was consistent with the position of the quasi-stationary front in the pre-summer rainy season (Figure 5b). It indicates that these RCs were mainly frontal precipitations, corresponding to medium rain top and inactive convection activity. RCs with mode of $TB_{10.4} > 265$ K were distributed quite uniformly in the study region—the proportion of warm-cloud precipitation over sea was higher than that over land (Figure 5c).

## 3.2 | Environmental conditions

In this section, we would like to investigate the general environmental conditions of the three classes of RCs to reveal their possible triggering mechanisms. Specifically, we used the total rainfall contribution of RC to perform weighted averages of environmental parameters, instead of using direct arithmetic averages.

Figure 6 shows the average distributions of 500 hPa geopotential height and winds, which is widely used to reveal the location of western Pacific subtropical high and fronts (Zhou *et al.*, 2009; Zhang *et al.*, 2020). As shown in Figure 6, during the pre-summer rainy season, the 500 hPa geopotential height and wind field for RCs with mode of $TB_{10.4}$ of 230–265 K was much different from that of <230 or >265 K. The area of subtropical high (with 500 hPa geopotential height >5,880 m) covered most of the southern regions south to 17°N on the map for RCs of 230–265 K (Figure 6b), whereas it only covered the southeast region near the Philippines for RCs of <230 or >265 K (Figure 6a,c). In the northern regions with latitude of ~29°N, the 500 hPa geopotential height was about 5,790 m for RCs of 230–265 K (Figure 6b), showing lower mid-level atmospheric pressure than that of <230 or >265 K with 500 hPa geopotential height about 5,810 m (Figure 6a,c).

Due to the southern stronger subtropical high and northern lower mid-level pressure, the mid-level pressure gradient in the study region was obviously larger for RCs with mode of $TB_{10.4}$ of 230–265 K than that of <230 or >265 K (Figure 6), resulting in much stronger fronts and westerly winds. As shown in Figure 6b, the strongest westerly winds occurred near the latitude of 26°N, indicating the location of quasi-stationary front over south China, which was also consistent with the location of precipitation samples (Figure 5b).
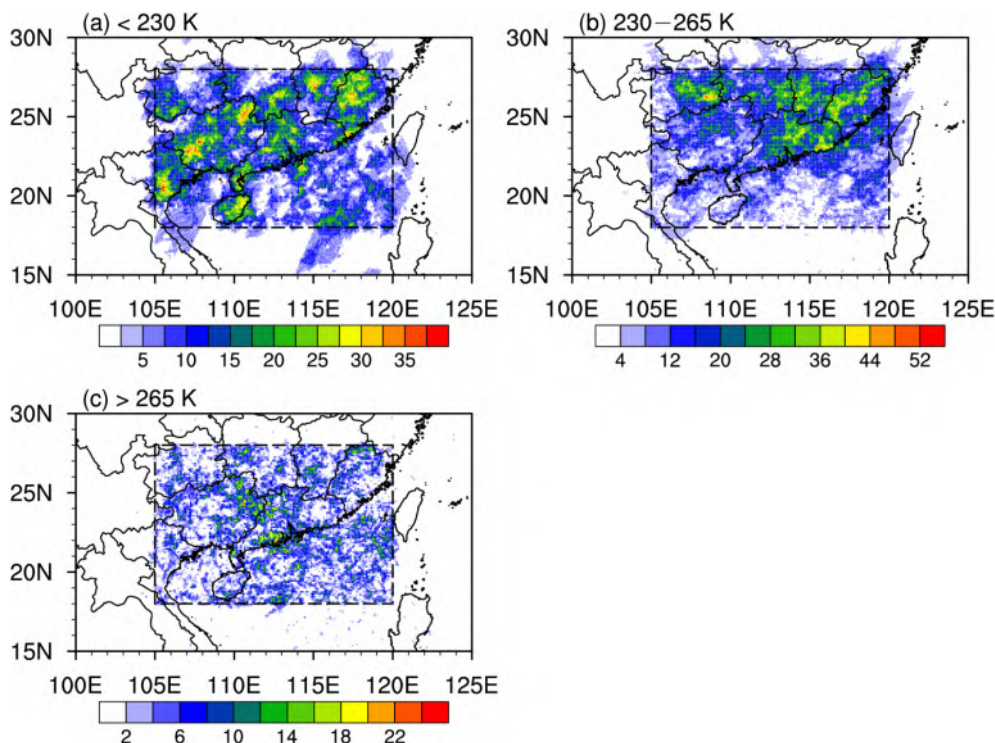
FIGURE 5 Horizontal distributions of precipitation sample sizes for RCs with mode of $TB_{10.4}$ at the range of (a) <230 K, (b) 230–265 K, and (c) >265 K, derived on $0.1° \times 0.1°$ grids from GPM 2ADPR for the pre-summer rainy season 2016–2020. The dashed rectangle indicates the study region [Colour figure can be viewed at wileyonlinelibrary.com]
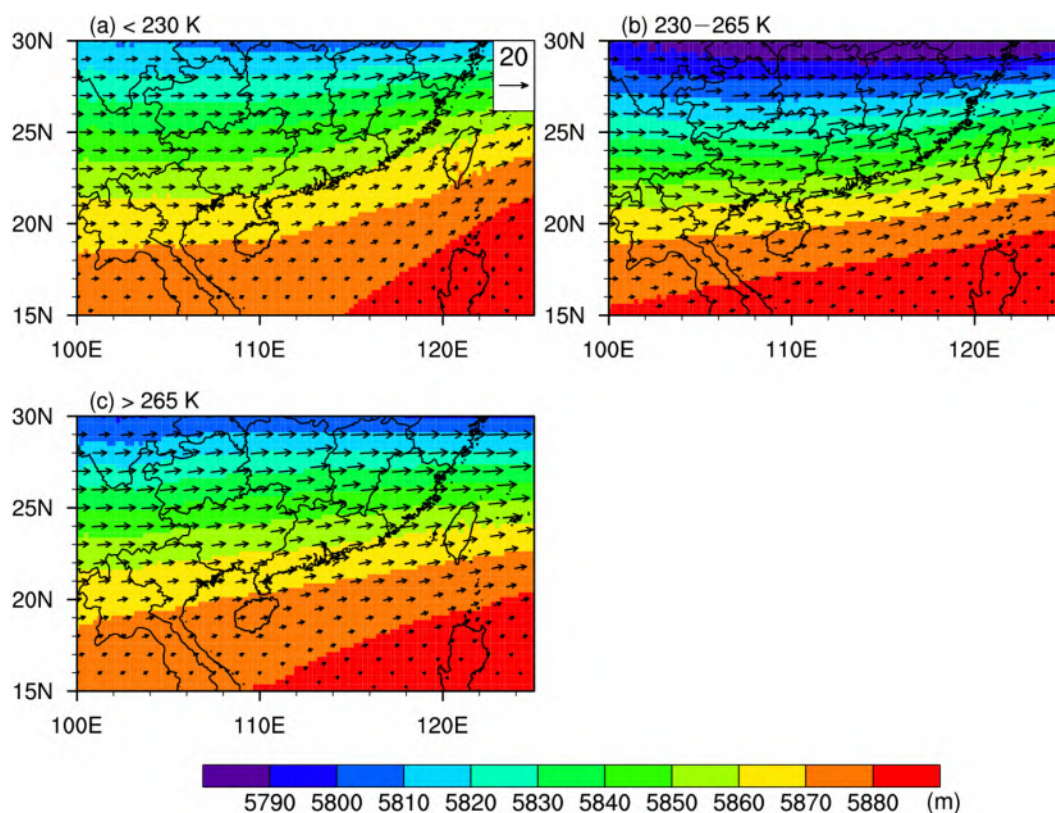


FIGURE 6 Horizontal distributions of 500 hPa geopotential height overlapped with wind field for three classes of RCs: (a) <230 K, (b) 230–265 K, and (c) >265 K, derived from ERA5 dataset. The figures were averaged based on rainfall contribution of RCs [Colour figure can be viewed at wileyonlinelibrary.com]
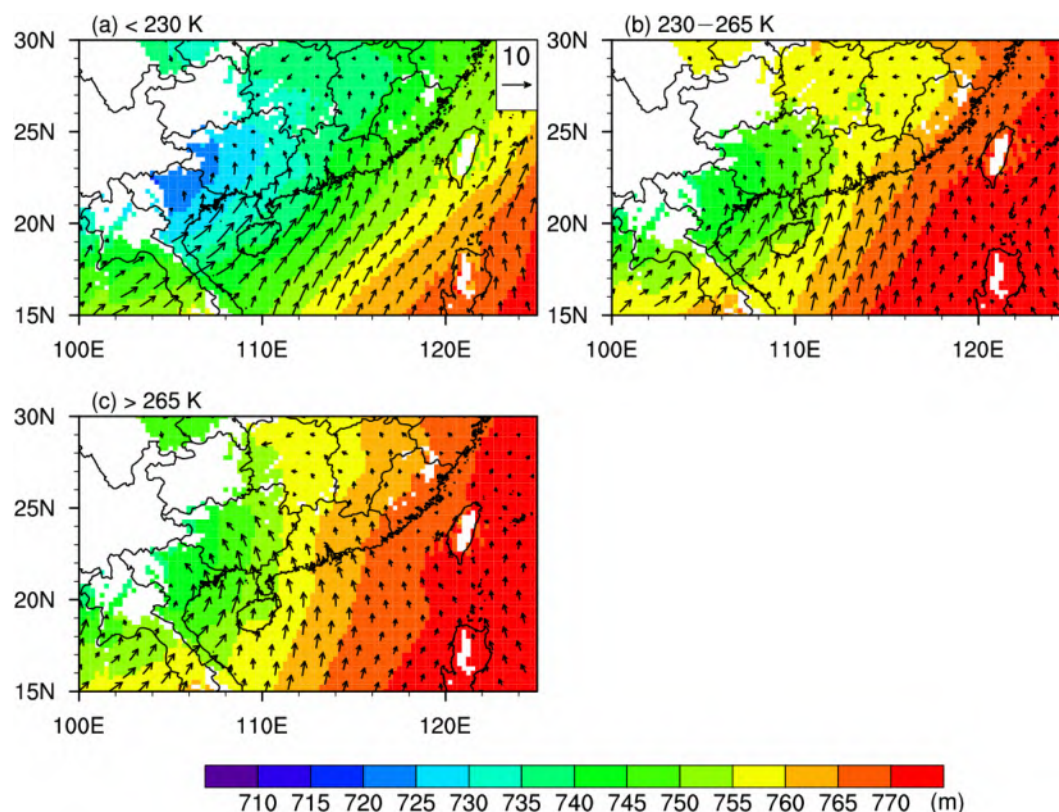
**FIGURE 7** The same as Figure 6, but for 925 hPa geopotential height overlapped with wind field. The white colour was used to indicate regions with elevation above 925 hPa geopotential height [Colour figure can be viewed at wileyonlinelibrary.com]

Unlike the 500 hPa environmental fields, the 925 hPa environmental fields showed obvious variances between RCs < 230 K (Figure 7a) and RCs > 230 K (Figure 7b,c). For RCs < 230 K, there existed a strong low-level vortex over Guizhou and northern Vietnam; the low-level high with 925 hPa geopotential height >765 m only controlled the southeast of map near the Philippines (Figure 7a). For RCs > 230 K, the low-level vortex was much weaker and the low-level high was much stronger that controlled most of the southeast oceanic regions on the map (Figure 7b,c). Due to the strong vortex for RCs < 230 K (Figure 7a), the 925 hPa winds over the coastal regions of south China showed as strong southwest winds, referred to the LLJ (Du and Chen, 2019; Sun et al., 2019), which was favour to the triggering of warm-sector heavy rainfall. For RCs > 230 K (Figure 7b,c), the strong winds only controlled the oceanic regions whereas the coastal regions over south China were dominated by southerly weaker winds.

For detailed knowledge on the environmental conditions of RCs < 230 K, we further investigated the latitude-vertical cross sections of wind field, equivalent potential temperature, and divergence (Figure 8). The coastal region is located from about 22°N to 25°N with clear increase of average terrain height. The regions between 18°N and 22°N are ocean regions while the regions between 25°N and 28°N are inland regions. Over

the ocean regions, the environmental conditions for RCs of <230 K and 230–265 K were similar. The low-level meridional wind for RCs of <230 K and 230–265 K exceeded 6 m·s$^{-1}$. The equivalent potential temperature decreased with increasing height till about 4 km, showing unstable low-level atmospheric layer (Figure 8a,b).

Over the coastal regions, the environmental conditions for variant classes of RCs were quite different. The low-level meridional wind was violent for RCs < 230 K, which validated the existence of LLJ (Figure 8a). The low-level atmospheric layer was unstable and the convergence zone extended from surface to 400 hPa, which resulted in strong updraft and therefore favoured convective activities (Figure 8a,d). On the contrary, the atmospheric layer was stable and the vertical wind was weak over the coastal regions for RCs at 230–265 K (Figure 8b,e), which suppressed intense convection activities.

Over the inland regions, due to the existence of fronts, the atmospheric layer was very stable for RCs at 230–265 K with average equivalent potential temperature of <330 K on the ground and ~340 K at 400 hPa level (Figure 8b). The meridional and vertical winds were weak, whereas the mid-level zonal winds were intense (Figure 6b).

The PDFs of CAPE and vertical interval of divergence of water vapour flux (div Q) was shown in Figure 9. As shown in the figure, both CAPE and div Q are less affected by
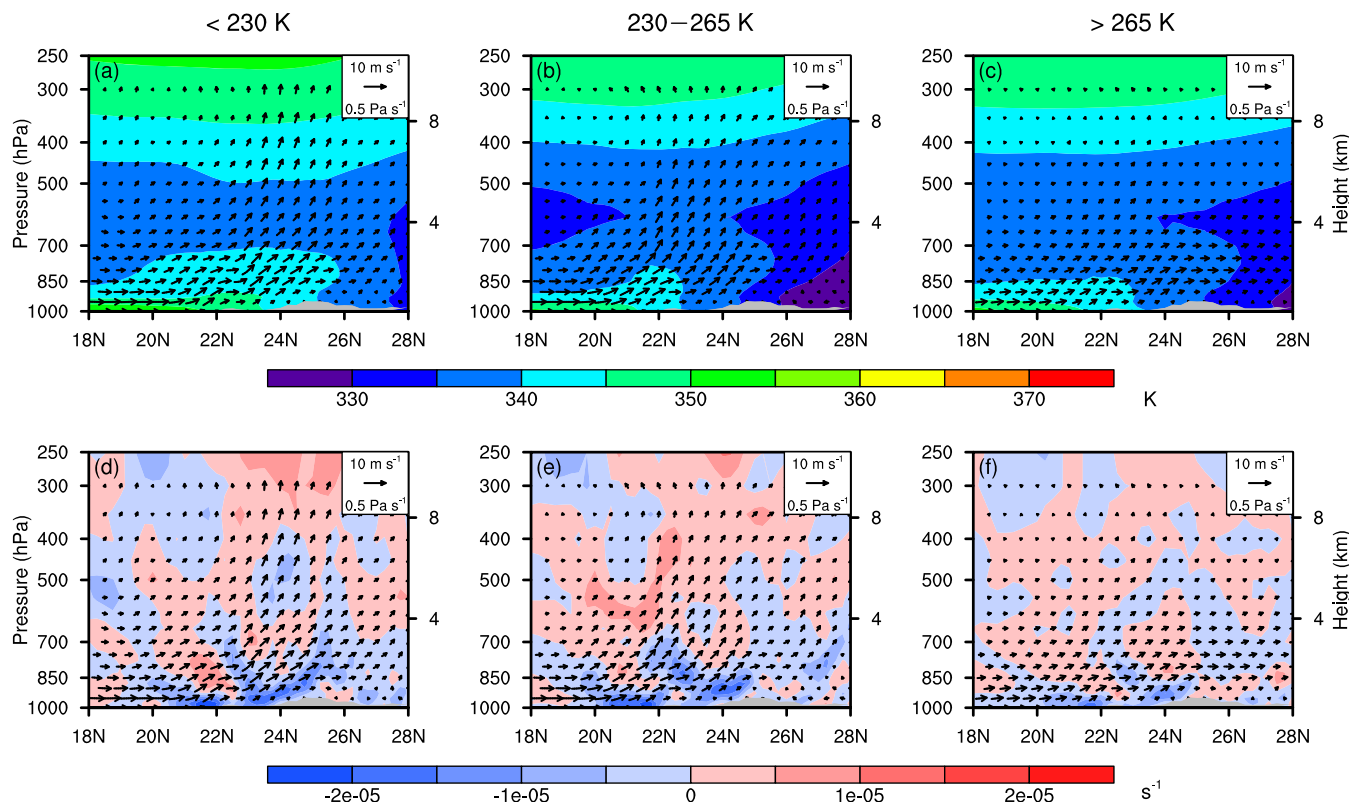
**FIGURE 8** South–north cross sections of latitude-vertical (a–c) equivalent potential temperature and (d–e) divergence, averaged between 111°E and 113°E for three classes of RCs. The shadowed area indicates the relative terrain height [Colour figure can be viewed at wileyonlinelibrary.com]

rain type. On the one hand, it is because the precipitation pixels with different rain type can be in the same RC with similar environmental conditions. On the other hand, it may also because the horizontal resolution of ERA5 data is 25 times of GPM 2ADPR and it is difficult to show the inner environment information of 2ADPR pixel. Both the two causes illustrate the need to study the environmental condition from the perspective of RC.

The PDFs of CAPE and div $Q$ were different among three classes of RCs (Figure 9). RCs with mode of $TB_{10.4} < 230$ K had the largest CAPE and strong convergence of water vapour flux, indicating unstable atmospheric layer and sufficient water supply, which was conducive to the occurrence of heavy convective precipitation. RCs with mode of $TB_{10.4}$ at 230–265 K had the smallest CAPE but strong convergence of water vapour flux, which was consistent to the environmental conditions of frontal precipitation like meiyu (Zhang et al., 2020). For RCs with mode of $TB_{10.4} > 265$ K, the divergence of water vapour flux was the largest indicating driest atmospheric layer; the CAPE was larger than that of 230–265 K. These showed that RCs with mode of $TB_{10.4} > 265$ K should be linked with the local convections, which often occurred in the afternoon with weak precipitation intensity.

In conclusion, RCs with mode of $TB_{10.4} < 230$ K were related to low-level vortex and LLJ. The atmosphere layer was very unstable and the water vapour transport was strong. These RCs included warm-sector heavy rainfall in the offshore area of south China. RCs with mode of $TB_{10.4}$ at 230–265 K were closely related to the quasi-stationary front with stable atmospheric layer and sufficient moisture supply. RCs with mode (peak) of $TB_{10.4} > 265$ K are mostly warm-cloud precipitations, also referred to warm rain in many studies, with storm-top height lower than the melting layer. As revealed by Kodama et al. (2009), warm rain tends to appear frequently over warm open sea and corresponds to the activity of stratocumulus. The local updraft plays important role in the triggering of shallow warm rain (Houze, 2014). During the pre-summer rainy season over south China, these RCs with mode of $TB_{10.4} > 265$ K contributes little to the total rainfall amount.

## 3.3 | Vertical structure and precipitation microphysics

Based on the three-dimensional detections of GPM DPR, we conducted investigations on the vertical structure and precipitation microphysics of RCs during the pre-summer
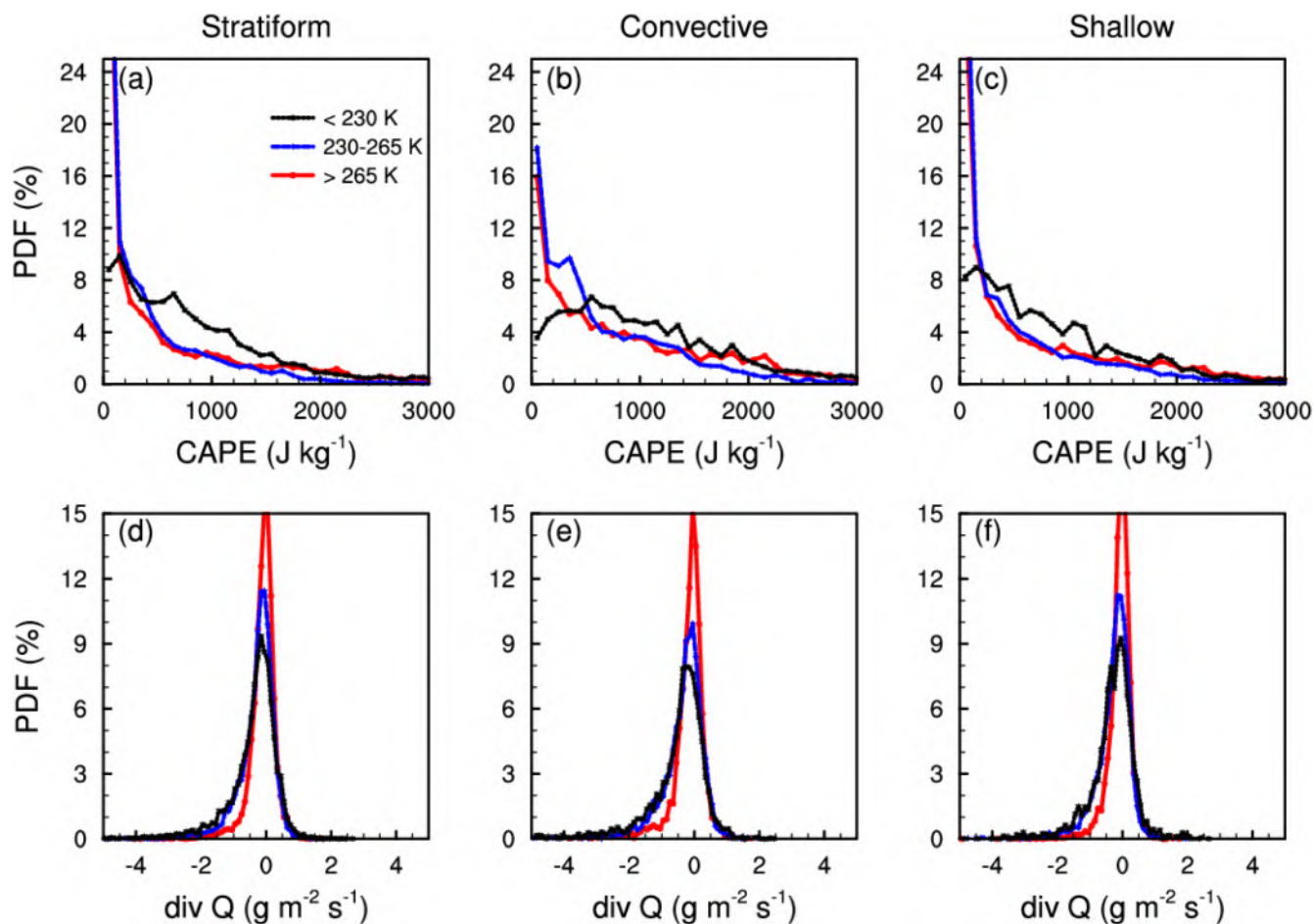
**FIGURE 9** PDFs of (a–c) CAPE and (d–f) vertical interval of divergence of water vapour flux (div $Q$) for three classes of RCs, derived from ERA5 dataset. The black, blue, and red lines indicate RCs with mode of $TB_{10.4}$ at the range of <230, 230–265, and >265 K, respectively. The spacings of CAPE and div $Q$ are 100 J·kg$^{-1}$ and 0.1 g·m$^{-1}$·s$^{-1}$, respectively [Colour figure can be viewed at wileyonlinelibrary.com]

rainy season over south China. First, we focused on the contoured frequency by altitude diagrams (CFADs) of Ku-band reflectivity with minimum detection threshold of 15.5 dBZ (Figure 10). The CFADs are normalized by the overall maximum.

The CFADs of stratiform precipitation showed different features for RCs of variant categories (Figure 10a–c). For RCs with mode of $TB_{10.4} < 230$ K, the vertical evolution of stratiform precipitation was concentrated above the melting layer with the outer contour (0.05) reaching 12 km (Figure 10a). The mode of Ku-band reflectivity reached 28 dBZ just above freezing level (~5 km), which was apparently larger than the other two classes (Figure 10b,c). For RCs of 230–265 K (Figure 10b), the CFAD of stratiform precipitation peaked at the area of (15.5–18 dBZ, 1–3 km), which was due to numerous weak stratiform precipitation with rain top below 4 km (Figure 4g). For RCs with mode of $TB_{10.4} > 265$ K (Figure 10c), the CFAD peaked near and just below the melting layer. The ice-

phased processes were less important for RCs of this category.

The liquid-phased precipitation microphysics are vital to the development of heavy precipitation (Kumjian and Prat, 2014). Yu *et al.* (2022) investigated the convective features of extreme precipitation with maximum radar reflectivity >40 dBZ over the Pearl River Delta. They found that the extreme precipitations are dominated by the coalescence in the liquid-phase processes rather than intense convection with presence of large solid precipitating particles. Although the CFADs of convective precipitation for the three classes were dramatically different above 0°C level, they were quite similar in the liquid zone below 4 km (Figure 10d,e). The small differences were manifested in the magnitude of near-surface echoes, with mode of 39, 37, and 36 dBZ for the three classes, respectively. The sort of near-surface echoes was consistent with convergence of moisture (Figure 9e). The CFADs of shallow precipitations within three classes of RCs were almost the same (Figure 10g–i).
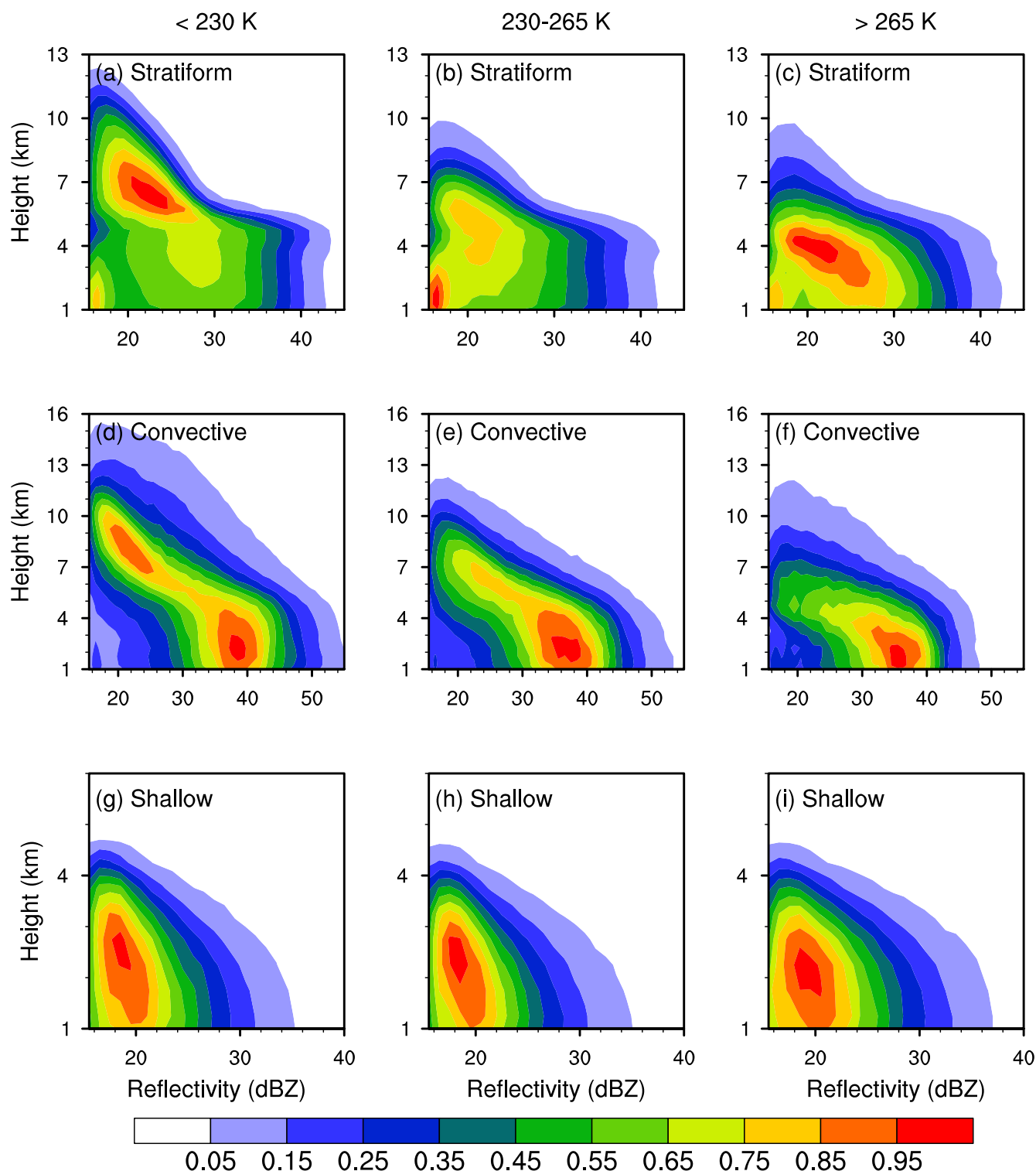
**FIGURE 10** CFADs of Ku-band corrected reflectivity for (a–c) stratiform, (d–f) convective, and (g–i) shallow precipitations within three classes of RCs. The spacings of x- and y-axis are 1 dBZ and 0.5 km, respectively [Colour figure can be viewed at wileyonlinelibrary.com]

Figure 11 shows the average profiles of DSD parameters, including $dBN_w$ ($10\log_{10}N_w$) indicating droplet density and effective droplet diameter ($D_m$). For any type of precipitation, RCs with mode of $TB_{10.4}$ at 230–265 K were companied with the largest $dBN_w$ and the smallest $D_m$

among all classes of RCs (Figure 11). This is because the RCs of this category were mainly frontal precipitation with abundant moisture supply but lack of updraft; small precipitation particles continuously generated in the low-to-mid layers. Due to lack of moisture supply, the $dBN_w$
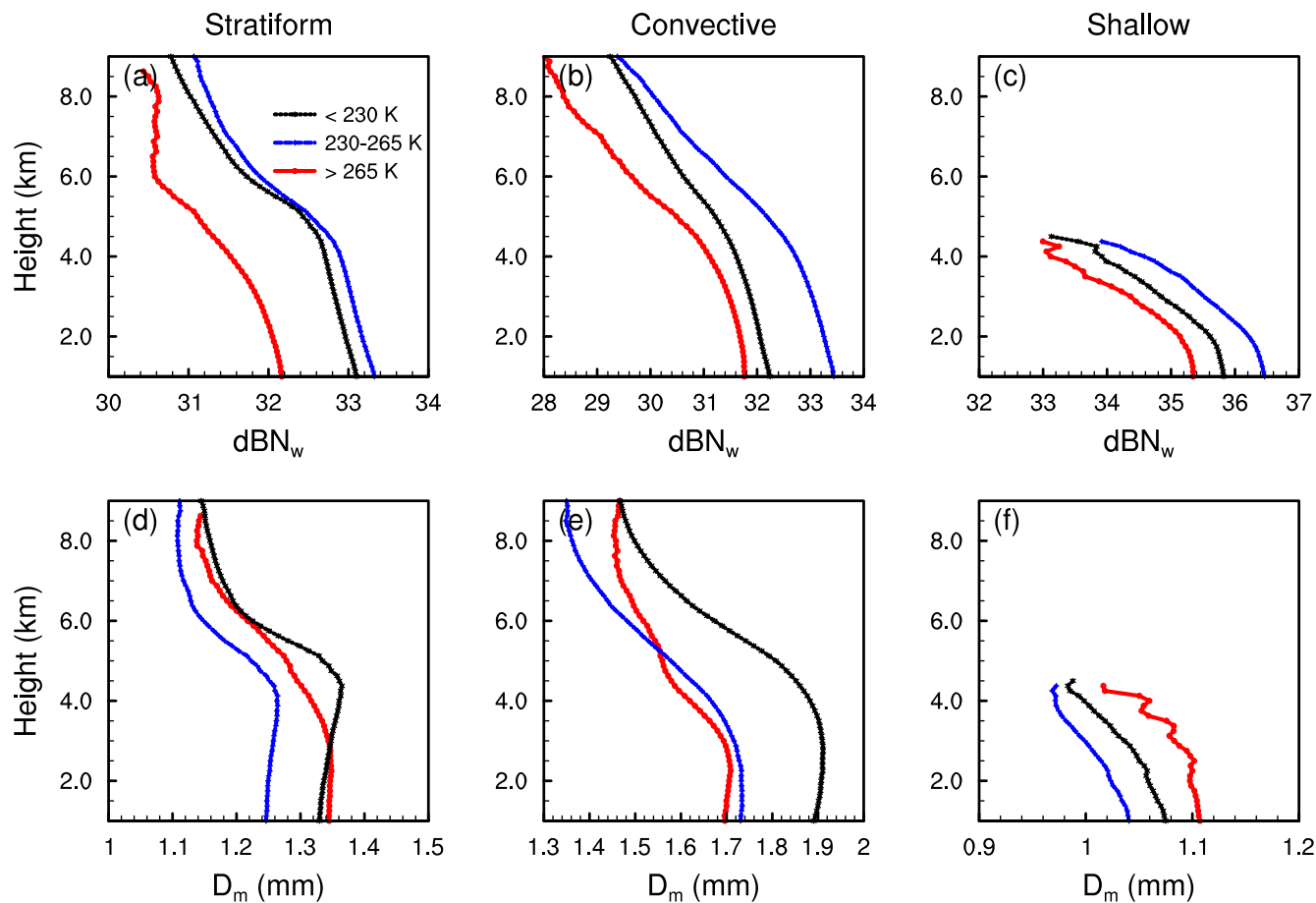
**FIGURE 11** Average profiles of (a–c) $dBN_w$ and (d–f) $D_m$ for three classes of RCs, derived from GPM 2ADPR dataset. The black, blue, and red lines indicate RCs with mode of $TB_{10.4}$ at the range of <230, 230–265, and >265 K, respectively. The vertical interval is 125 m [Colour figure can be viewed at wileyonlinelibrary.com]

of RCs with mode of $TB_{10.4} > 265$ K was the smallest of all classes (Figure 11a–c).

For stratiform precipitations, the main growth modes of particles are known to be the ice-phased processes including deposition, riming, and aggregation (Houze, 2014). When particles fall to the melting layer, they will get smaller due to melting process, corresponding to the turning point of $D_m$ profile at around 4.5 km (Figure 11d). This turning point was not obvious for RCs with mode of $TB_{10.4} > 265$ K due to the low rain top. The $D_m$ for RCs with mode of $TB_{10.4} < 230$ K was 0.06–0.1 mm larger than that of 230–265 K at all heights, which was suggested to be resulted from two aspects. One is that the higher rain top provided a longer path for ice particles to grow; the other is the mid-level updraft restricted the falling of small particles.

For convective precipitations, there is no uniform melting level within clouds due to convection activity (Houze, 1997). Under the lift of updraft, the particles need to grow larger before falling to ground. Therefore, the $D_m$ of convective precipitation was much larger than that of stratiform precipitation (Figure 11d,e). RCs with mode of $TB_{10.4} < 230$ K had the largest $D_m$ with a value of 1.9 mm at 1 km height due to the strongest updraft (Figure 11e).

For shallow precipitations, the DSD profiles of the three classes of RCs showed distinct characteristics despite similar CFADs. RCs with mode of $TB_{10.4}$ at 230–265 K had the largest $dBN_w$ but smallest $D_m$, whereas it was just the opposite for RCs with mode of $TB_{10.4} > 265$ K. We suggest it is because the ratio of shallow precipitation was low when mode of $TB_{10.4} < 265$ K; therefore, shallow pixel was likely to be affected by its surrounding rainfall pixels. The reasons why shallow precipitations occasionally appear in deep precipitation clouds still needs to be analysed through high-precision models and observations.

## 4 | DISCUSSION AND CONCLUSIONS

In this work, we investigate the triggering mechanism, horizontal distribution, and vertical microphysics of precipitation during the pre-summer rainy season over south China from the perspective of precipitation events. We first identified RCs from GPM 2ADPR dataset, and then conducted taxonomy researches based on the mode of

Himawari-8 AHI $TB_{10.4}$ of RCs. By analysing the differences in rain type, near-surface rain rate, storm-top height and other precipitation features of RCs with variant mode of $TB_{10.4}$, RCs were classified into three classes: <230, 230–265, and >265 K. The three classes of RCs had distinct characteristics as follows:

1. RCs with mode of $TB_{10.4} < 230$ K. These RCs contributed 51.5% of total rainfall amount during the pre-summer rainy season over south China. RCs were mainly distributed in the offshore regions and contained warm-sector heavy rainfall; low-level vortex and offshore LLJ were vital triggers for them. The environmental atmospheric layer was very unstable with sufficient moisture supply. Affected by this, the ratio of convective precipitation was the highest among three classes with high rain top and heavy rain rate. Specifically, under the lift of strong updraft, the $D_m$ of convective precipitation for RCs with mode of $TB_{10.4} < 230$ K far exceeded the other two classes with a mean value of ~1.9 mm below 0°C level, which is like the average $D_m$ of extreme precipitations (1.89 mm) over the Pearl River Delta (Yu *et al.*, 2022). However, the average $dBN_w$ of convective precipitation for RCs with mode of $TB_{10.4} < 230$ K (~32.2) was significantly lower than extreme precipitations (~39.8), showing that there was more prominent coalescence warm-rain process for the triggering of extreme events.

2. RCs with mode of $TB_{10.4}$ at 230–265 K. Despite the low cloud top, these RCs contributed around 39.8% of the total rainfall amount. This result supported that many extreme precipitation events are produced by relatively weak convective systems (Xu *et al.*, 2022). RCs with mode of $TB_{10.4}$ at 230–265 K were related to the quasi-stationary front over south China; therefore, they were distributed near the average location of front at 23°–27°N. The mid-level pressure gradient over the study region and westerly winds were significantly stronger than the other two classes. The atmospheric layer was quite stable with sufficient moisture supply, so stratiform precipitation dominated the RCs. The mode of near-surface rain rate within stratiform precipitation was only ~0.3 mm·hr$^{-1}$, indicating they were continuous light rain. Below 3 km, numerous small droplets continuously formed under strong water vapour flux, so the droplet density was high whereas the $D_m$ was small.

3. RCs with mode of $TB_{10.4} > 265$ K. These RCs were mainly warm-cloud precipitation, which account for only 8.7% of the total rainfall amount. The number of RCs was large but the scale was small. They were distributed quite uniformly in the study region; the proportion over sea was larger than that over land. RCs were triggered by the local convections and dominated by shallow precipitation. The atmospheric layer was quite unstable with insufficient moisture flux. Therefore, RCs of this class had the lowest droplet density and large $D_m$.

The uncertainties of the study include the follows. Due to the large spatiotemporal scale of this study, we did not carry out one-by-one analysis on the environmental condition of the RCs. In the future, we will target on subregions with frequent precipitation and conduct detailed analysis using objective synoptic classification and high-resolution simulation to establish microphysical parameterization schemes for RCs of each category.

## DATA AVAILABILITY STATEMENT

The GPM 2ADPR data used in this study was collected from the Precipitation Measurement Mission website (https://pmm.nasa.gov). The Himawari-8 AHI data was provided by the Japanese Meteorological Agency (http://www.data.jma.go.jp/mscweb/en/himawari89/). The ERA5 reanalysis data used in this study was collected from the ECMWF website (https://apps.ecmwf.int/).

## ORCID

*Yilun Chen* https://orcid.org/0000-0002-9134-9368

## REFERENCES

Bai, L., Chen, G. and Huang, L. (2020) Convection initiation in monsoon coastal areas (south China). *Geophysical Research Letters*, 47, e2020GL087035. https://doi.org/10.1029/2020GL087035.

Chen, G., Sha, W. and Iwasaki, T. (2009) Diurnal variation of precipitation over southeastern China: spatial distribution and its seasonality. *Journal of Geophysical Research*, 114, D13103. https://doi.org/10.1029/2008JD011103.

Chen, X., Zhao, K. and Xue, M. (2014) Spatial and temporal characteristics of warm season convection over Pearl River Delta region, China, based on 3 years of operational radar data. *Journal of Geophysical Research: Atmospheres*, 119, 12447–12465. https://doi.org/10.1002/2014JD021965.

Chen, Y., Zhang, A., Fu, Y., Chen, S. and Li, W. (2021) Morphological characteristics of precipitation areas over the Tibetan Plateau measured by TRMM PR. *Advances in Atmospheric Sciences*, 38(4), 677–689. https://doi.org/10.1007/s00376-020-0233-1.

Curtis, S. (2019) Means and long-term trends of global coastal zone precipitation. *Scientific Reports*, 9(1), 5401. https://doi.org/10.1038/s41598-019-41878-8.

Da, C. (2015). Preliminary assessment of the Advanced Himawari Imager (AHI) measurement onboard Himawari&hyphen;8 geostationary satellite. *Remote Sensing Letters*, 6(8), 637–646. https://doi.org/10.1080/2150704x.2015.1066522.

Ding, Y. and Chan, J.C.L. (2005) The East Asian summer monsoon: an overview. *Meteorology and Atmospheric Physics*, 89(1–4), 117–142. https://doi.org/10.1007/s00703-005-0125-z.

Du, Y. and Chen, G. (2019) Heavy rainfall associated with double low-level jets over southern China. Part II: convection initiation. *Monthly Weather Review*, 147(2), 543–565. https://doi.org/10.1175/MWR-D-18-0102.1.

Du, Y. and Rotunno, R. (2018) Diurnal cycle of rainfall and winds near the south coast of China. *Journal of the Atmospheric Sciences*, 75(6), 2065–2082. https://doi.org/10.1175/JAS-D-17-0397.1.

Fiolleau, T. and Roca, R. (2013) Composite life cycle of tropical mesoscale convective systems from geostationary and low Earth orbit satellite observations: method and sampling considerations. *Quarterly Journal of the Royal Meteorological Society*, 139, 941–953.

Fu, Y., Chen, Y., Zhang, X., Wang, Y., Li, R., Liu, Q., Zhong, L., Zhang, Q. and Zhang, A. (2021) Fundamental characteristics of tropical rain cell structures as measured by TRMM PR. *Journal of Meteorological Research*, 34(6), 1129–1150. https://doi.org/10.1007/s13351-020-0035-5.

Gu, X., Zhang, Q., Singh, V.P., Liu, L. and Shi, P. (2017) Spatiotemporal patterns of annual and seasonal precipitation extreme distributions across China and potential impact of tropical cyclones. *International Journal of Climatology*, 37(10), 3949–3962. https://doi.org/10.1002/joc.4969.

Han, B., du, Y., Wu, C. and Liu, X. (2021) Microphysical characteristics of the coexisting frontal and warm-sector heavy rainfall in south China. *Journal of Geophysical Research: Atmospheres*, 126, e2021J–e35446J. https://doi.org/10.1029/2021JD035446.

Hanna, J.W., Schultz, D.M. and Irving, A.R. (2008) Cloud-top temperatures for precipitating winter clouds. *Journal of Applied Meteorology and Climatology*, 47(1), 351–359. https://doi.org/10.1175/2007JAMC1549.1.

Hersbach, H., Bell, B., Berrisford, P., Hirahara, S., Horányi, A., Muñoz-Sabater, J., Nicolas, J., Peubey, C., Radu, R., Schepers, D., Simmons, A., Soci, C., Abdalla, S., Abellan, X., Balsamo, G., Bechtold, P., Biavati, G., Bidlot, J., Bonavita, M., Chiara, G., Dahlgren, P., Dee, D., Diamantakis, M., Dragani, R., Flemming, J., Forbes, R., Fuentes, M., Geer, A., Haimberger, L., Healy, S., Hogan, R.J., Hólm, E., Janisková, M., Keeley, S., Laloyaux, P., Lopez, P., Lupu, C., Radnoti, G., Rosnay, P., Rozum, I., Vamborg, F., Villaume, S. and Thépaut, J.N. (2020) The ERA5 global reanalysis. *Quarterly Journal of the Royal Meteorological Society*, 146(730), 1999–2049. https://doi.org/10.1002/qj.3803.

Houze, R.A. (1997) Stratiform precipitation in regions of convection: a meteorological paradox? *Bulletin of the American Meteorological Society*, 78(10), 2179–2196. https://doi.org/10.1175/1520-0477(1997)078<2179:SPIROC>2.0.CO;2.

Houze, R.A. (2014). *Cloud Dynamics*. Oxford: Academic Press.

Huo, Z., Ruan, Z., Wei, M., Ge, R., Li, F. and Ruan, Y. (2019) Statistical characteristics of raindrop size distribution in south China summer based on the vertical structure derived from VPR-CFMCW. *Atmospheric Research*, 222, 47–61. https://doi.org/10.1016/j.atmosres.2019.01.022.

Jiang, Z., Zhang, D.L., Xia, R. and Qian, T. (2017) Diurnal variations of Presummer rainfall over southern China. *Journal of Climate*, 30(2), 755–773. https://doi.org/10.1175/JCLI-D-15-0666.1.

Kodama, Y., Katsumata, M., Mori, S., Satoh, S., Hirose, Y. and Ueda, H. (2009) Climatology of warm rain and associated latent heating derived from TRMM PR observations. *Journal of Climate*, 22(18), 4908–4929. https://doi.org/10.1175/2009JCLI2575.1.

Kumjian, M.R. and Prat, O.P. (2014) The impact of raindrop collisional processes on the Polarimetric radar variables. *Journal of the Atmospheric Sciences*, 71(8), 3052–3067. https://doi.org/10.1175/JAS-D-13-0357.1.

Lau, K. and Wu, H. (2010) Characteristics of precipitation, cloud, and latent heating associated with the Madden–Julian oscillation. *Journal of Climate*, 23(3), 504–518. https://doi.org/10.1175/2009JCLI2920.1.

Li, N., Wang, Z., Chen, X. and Austin, G. (2019) Studies of general precipitation features with TRMM PR data: an extensive overview. *Remote Sensing*, 11(1), 80. https://doi.org/10.3390/rs11010080.

Li, X. and Du, Y. (2021) Statistical relationships between two types of heavy rainfall and low-level jets in south China. *Journal of Climate*, 34(21), 8549–8566. https://doi.org/10.1175/JCLI-D-21-0121.1.

Liu, C. and Zipser, E.J. (2015) The global distribution of largest, deepest, and most intense precipitation systems. *Geophysical Research Letters*, 42(9), 3591–3595. https://doi.org/10.1002/2015GL063776.

Liu, L., Ding, Z., Chang, Y. and Chen, M. (2012) Application of parameterization of orographic gravity wave drag in WRF model to mechanism analysis of a heavy rain in warm sector over south China. *Meteorological Science and Technology*, 40, 232–240. https://doi.org/10.3969/j.issn.1671-6345.2012.02.017.

Luo, Y., Wan, Q., Wang, B., Wong, W.K., Hu, Z., Jou, B.J., Lin, Y., Johnson, R.H., Chang, C., Zhu, Y., Zhang, X., Wang, H., Xia, R., Ma, J., Zhang, D., Gao, M., Zhang, Y., Liu, X., Chen, Y., Huang, H., Bao, X., Ruan, Z., Cui, Z., Meng, Z., Sun, J., Wu, M., Wang, H., Peng, X., Qian, W., Zhao, K. and Xiao, Y. (2017) The southern China monsoon rainfall experiment (SCMREX). *Bulletin of the American Meteorological Society*, 98(5), 999–1013. https://doi.org/10.1175/BAMS-D-15-00235.1.

Luo, Y., Xia, R. and Chan, J.C.L. (2020) Characteristics, physical mechanisms, and prediction of pre-summer rainfall over south China: research Progress during 2008–2019. *Journal of the meteorological Society of Japan Ser. II*, 98(1), 19–42. https://doi.org/10.2151/jmsj.2020-002.

Nesbitt, S.W., Cifelli, R. and Rutledge, S.A. (2006) Storm morphology and rainfall characteristics of TRMM precipitation features. *Monthly Weather Review*, 134(10), 2702–2721. https://doi.org/10.1175/MWR3200.1.

Rao, K.G. and Reddy, N.N. (2019) On moisture flux of the Indian summer monsoon: a new perspective. *Geophysical Research Letters*, 46, 1794–1804. https://doi.org/10.1029/2018GL080392.

Seto, S., Iguchi, T., Meneghini, R., Awaka, J., Kubota, T., Masaki, T. and Takahashi, N. (2021) The precipitation rate retrieval algorithms for the GPM dual-frequency precipitation radar. *Journal of the Meteorological Society of Japan Ser. II*, 99(2), 205–237. https://doi.org/10.2151/jmsj.2021-011.

Sun, J., Zhang, Y., Liu, R., Fu, S. and Tian, F. (2019) A review of research on warm-sector heavy rainfall in China. *Advances in Atmospheric Sciences*, 36(12), 1299–1307. https://doi.org/10.1007/s00376-019-9021-1.

Tao, S. and Chen, L. (1987) A review of recent research on the East Asian summer monsoon in China. In: *Monsoon Meteorology*. Oxford: Oxford University Press, pp. 60–92.

Weckwerth, T.M. and Wakimoto, R.M. (1992) The initiation and organization of convective cells atop a cold-air outflow boundary. *Monthly Weather Review*, 120, 2169–2187. https://doi.org/10.1175/1520-0493(1992)120<2169:TIAOOC>2.0.CO;2.

Wu, N., Ding, X., Wen, Z., Chen, G., Meng, Z., Lin, L. and Min, J. (2020) Contrasting frontal and warm-sector heavy rainfalls over south China during the early-summer rainy season. *Atmospheric Research*, 235, 104693. https://doi.org/10.1016/j.atmosres.2019.104693.

Xu, W., Chen, H., Wei, H., Luo, Y. and Zhao, T. (2022) Extreme precipitation produced by relatively weak convective systems in the Tropics and subtropics. *Geophysical Research Letters*, 49(7), e2022GL098048. https://doi.org/10.1029/2022GL098048.

Xu, W., Zipser, E.J., Chen, Y.L., Liu, C., Liou, Y.C., Lee, W.C. and Jong-Dao Jou, B. (2012) An orography-associated extreme rainfall event during TiMREX: initiation, storm evolution, and maintenance. *Monthly Weather Review*, 140(8), 2555–2574. https://doi.org/10.1175/MWR-D-11-00208.1.

Yu, R., Zhou, T., Xiong, A., Zhu, Y. and Li, J. (2007) Diurnal variations of summer precipitation over contiguous China. *Geophysical Research Letters*, 34(1), L01704. https://doi.org/10.1029/2006GL028129.

Yu, S., Luo, Y., Wu, C., Zheng, D., Liu, X. and Xu, W. (2022) Convective and microphysical characteristics of extreme precipitation revealed by multisource observations over the Pearl River Delta at monsoon coast. *Geophysical Research Letters*, 49(2), e2021GL097043. https://doi.org/10.1029/2021GL097043.

Zhang, A. and Fu, Y. (2018) Life cycle effects on the vertical structure of precipitation in east China measured by Himawari-8 and GPM DPR. *Monthly Weather Review*, 146(7), 2183–2199. https://doi.org/10.1175/MWR-D-18-0085.1.

Zhang, A., Chen, C., Chen, Y., Li, W., Chen, S. and Fu, Y. (2022) Resilient dataset of rain clusters with life cycle evolution during April to June 2016–2020 over eastern Asia based on observations from the GPM DPR and Himawari-8 AHI. *Earth System Science Data*, 14(3), 1433–1445. https://doi.org/10.5194/essd-14-1433-2022.

Zhang, A., Chen, Y., Zhou, S., Cui, C., Wan, R. and Fu, Y. (2020) Diurnal variation of Meiyu rainfall in the Yangtze plain during atypical Meiyu years. *Journal of Geophysical Research: Atmospheres*, 125(1), e2019JD031742. https://doi.org/10.1029/2019JD031742.

Zhang, Q., Gu, X., Singh, V.P., Shi, P. and Luo, M. (2017) Timing of floods in southeastern China: seasonal properties and potential causes. *Journal of Hydrology*, 552, 732–744. https://doi.org/10.1016/j.jhydrol.2017.07.039.

Zheng, J., Liu, L., Chen, H., Gou, Y., Che, Y., Xu, H. and Li, Q. (2019) Characteristics of warm clouds and precipitation in south China during the pre-flood season using datasets from a cloud radar, a ceilometer, and a disdrometer. *Remote Sensing*, 11(24), 3045. https://doi.org/10.3390/rs11243045.

Zhou, T., Yu, R., Zhang, J., Drange, H., Cassou, C., Deser, C., Hodson, D.L.R., Sanchez-Gomez, E., Li, J., Keenlyside, N., Xin, X. and Okumura, Y. (2009) Why the Western Pacific subtropical high has extended westward since the late 1970s. *Journal of Climate*, 22(8), 2199–2215. https://doi.org/10.1175/2008JCLI2527.1.